# Supplementary Information

## Confining Hollow ZnSe/NiSe Microspheres in Freestanding Carbon Nanofibers for Flexible Potassium-Ion Batteries

Bo Yan,[a] Hao Sun,[c] Xueping Liu,[b] Xinyuan Fu,[c] Changqing Xu,[c] Tiantian Zhang,[c] Huachao Tao,[a] Lulu Zhang,[c] Xifei Li,[d] Xuelin Yang,*[a] Renheng Wang*[b]

[a]*College of Materials and Chemical Engineering, China Three Gorges University, Yichang 443002, P. R. China.*

[b]*Key Laboratory of Optoelectronic Devices and Systems of Ministry of Education and Guangdong Province, State Key Laboratory of Radio Frequency Heterogeneous Integration (Shenzhen University), College of Physics and Optoelectronic Engineering, Shenzhen University, Shenzhen 518060, P.R. China.*

[c]*Collaborative Innovation Center for Microgrid of New Energy, College of Electrical Engineering & New Energy, China Three Gorges University, Yichang 443002, P. R. China.*

[d]*Xi'an Key Laboratory of New Energy Materials and Devices, Institute of Advanced Electrochemical Energy & School of Materials Science and Engineering, Xi'an University of Technology, Xi'an 710048, P. R. China.*

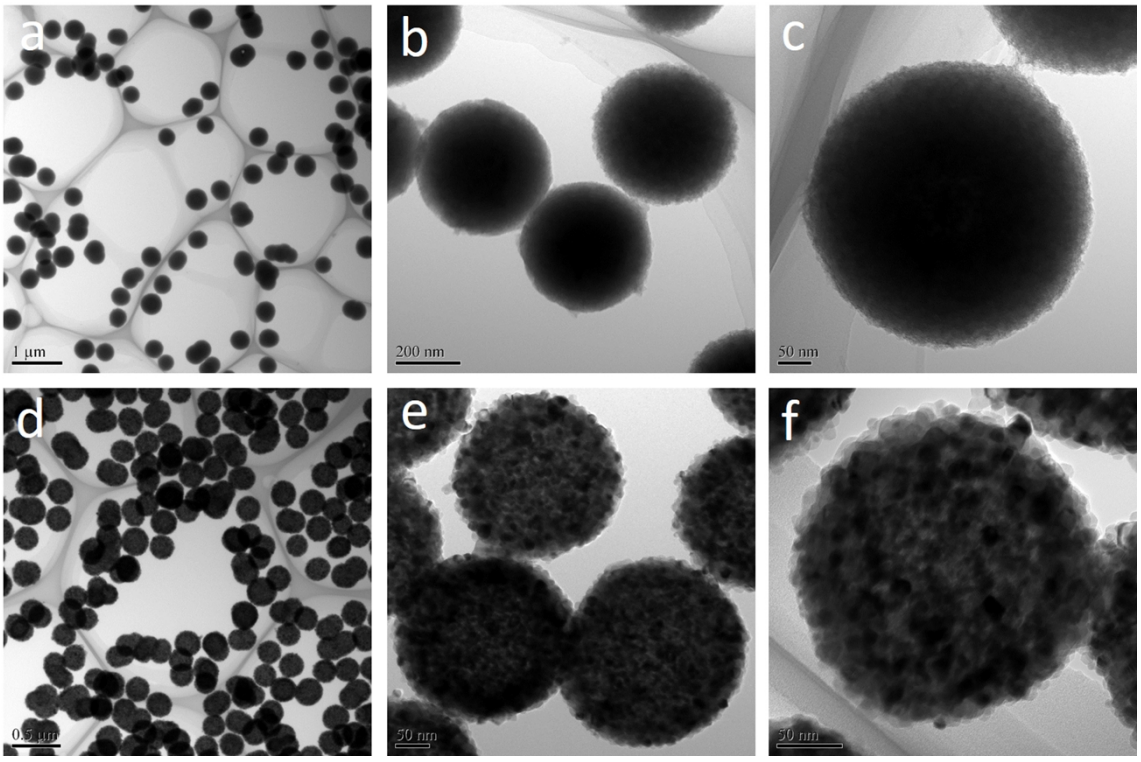


**Fig. S1** TEM of (a-c) ZnNi-P, and (d-f) ZnNi-P after annealing at 700 °C in air, showing the non-hollow structure.

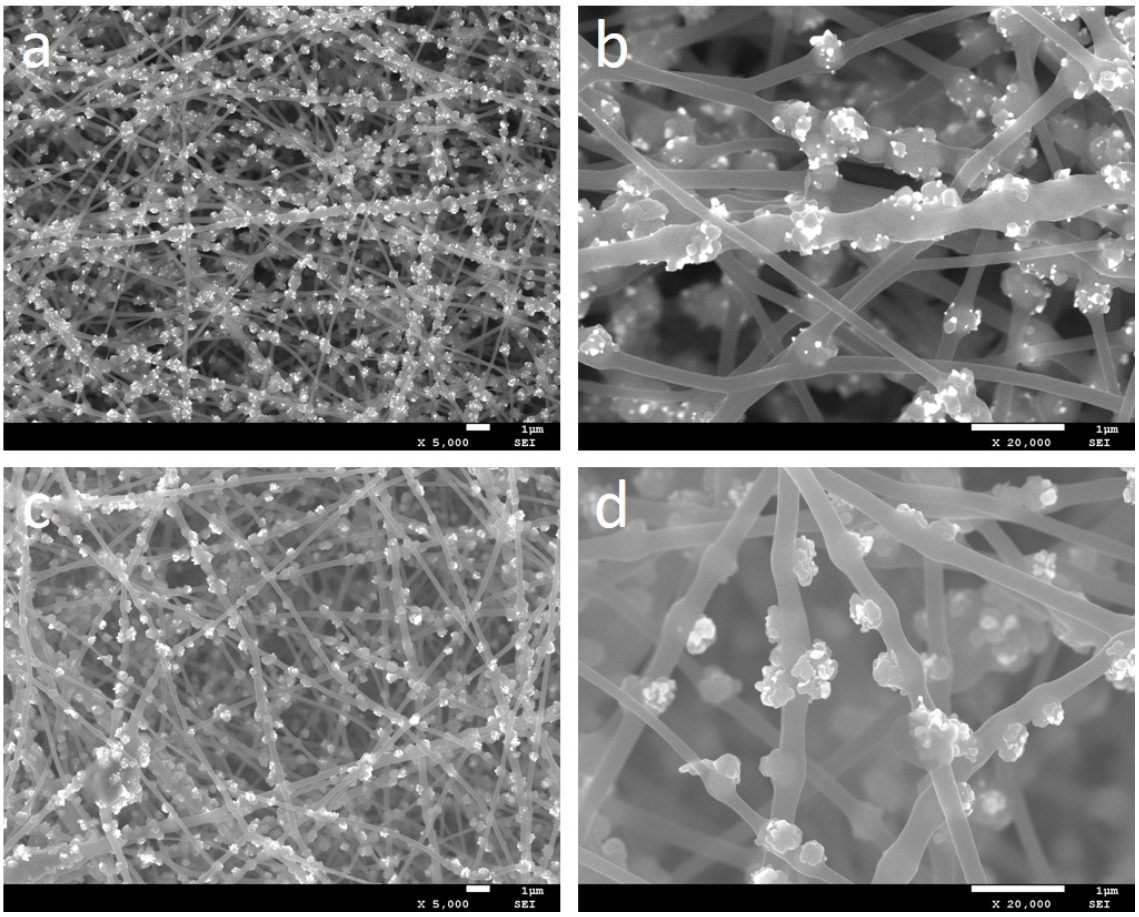


**Fig. S2** SEM images of the obtained ZnSe/NiSe@NC films synthesized by (a, b) 100 mg Se powder and (c, d) 50 mg Se powder upstream in the tube furnace and pre-oxidized nanofibers containing 160 mg of ZnNi-P downstream in the tube furnace.

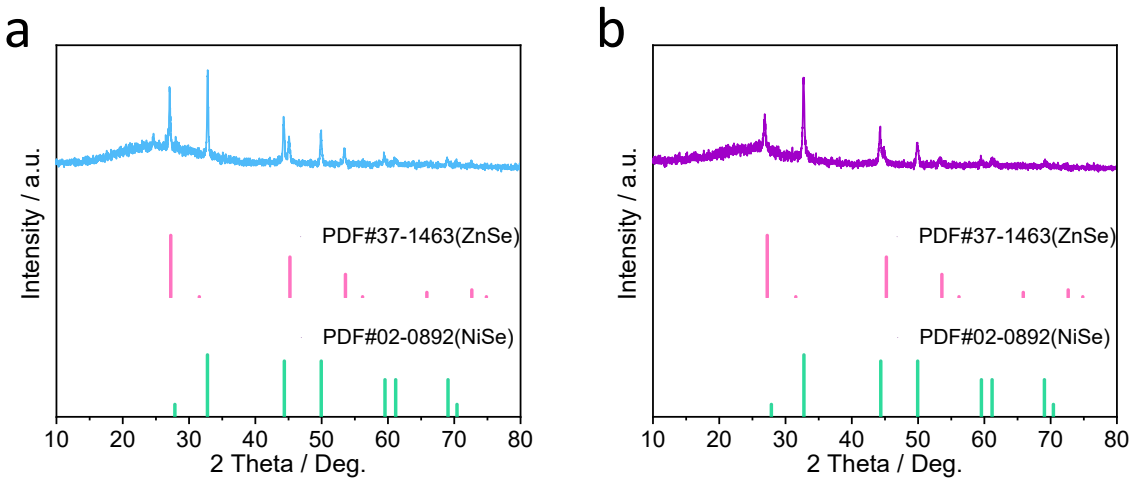


**Fig. S3** Comparison the phase of ZnSe/NiSe@NC materials prepared by (a) improved and (b) conventional selenization methods.

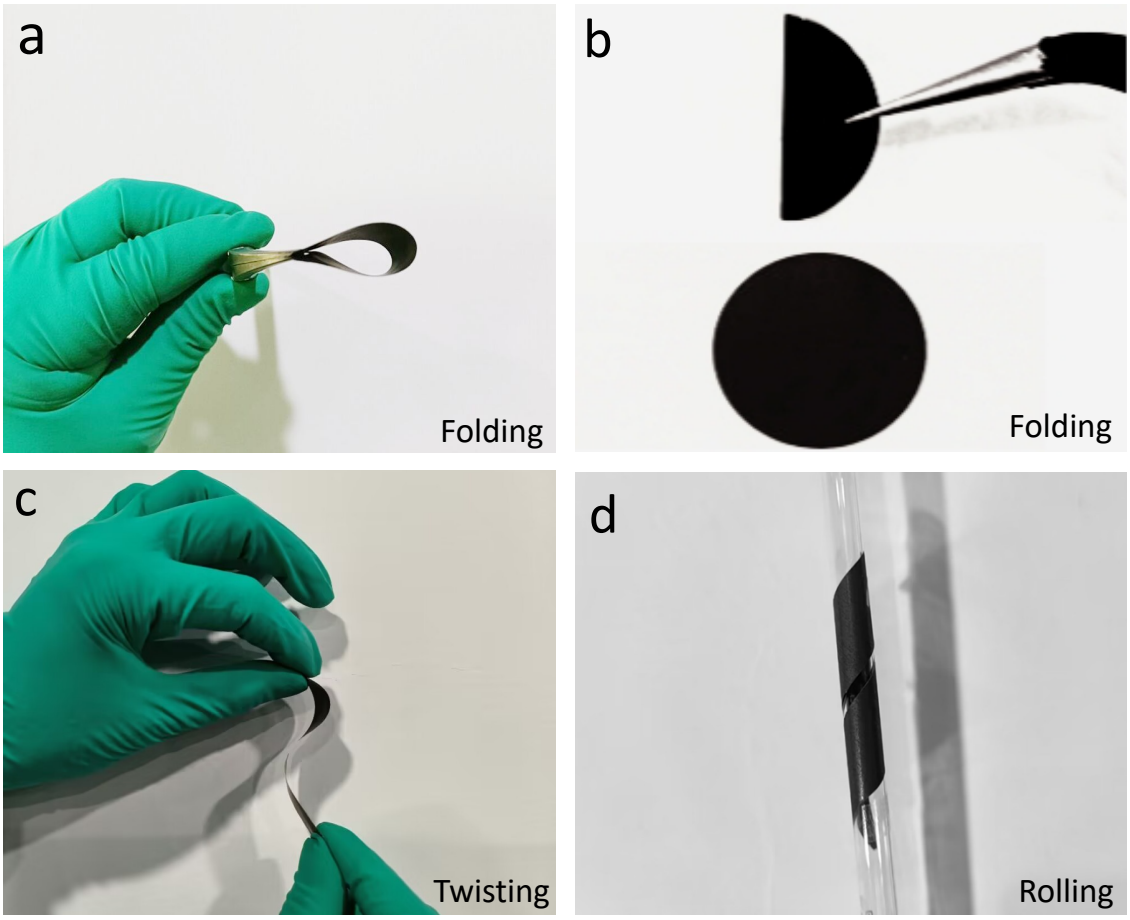


**Fig. S4** Demonstration of the flexible characteristic of ZnSe/NiSe@NC.

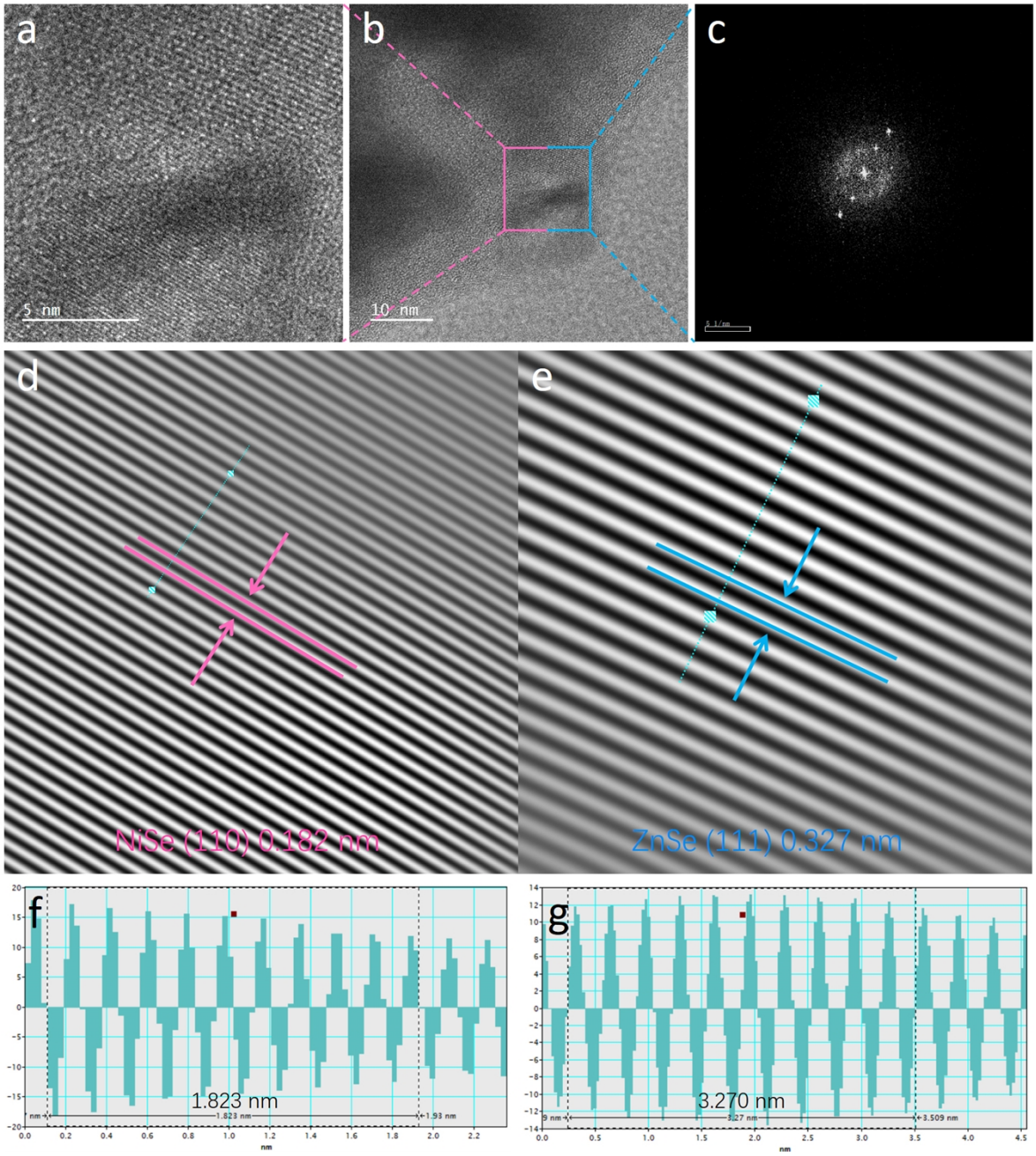


**Fig. S5** Typical structural characterizations of ZnSe/NiSe heterojunctions. (a) Magnified HRTEM image and (c) live Fast Fourier Transformation (FFT) pattern of the selected area labeled in (b). (d, e) The Inverse FFT (IFFT) patterns and (f, g) corresponding IFFT liner profiles.

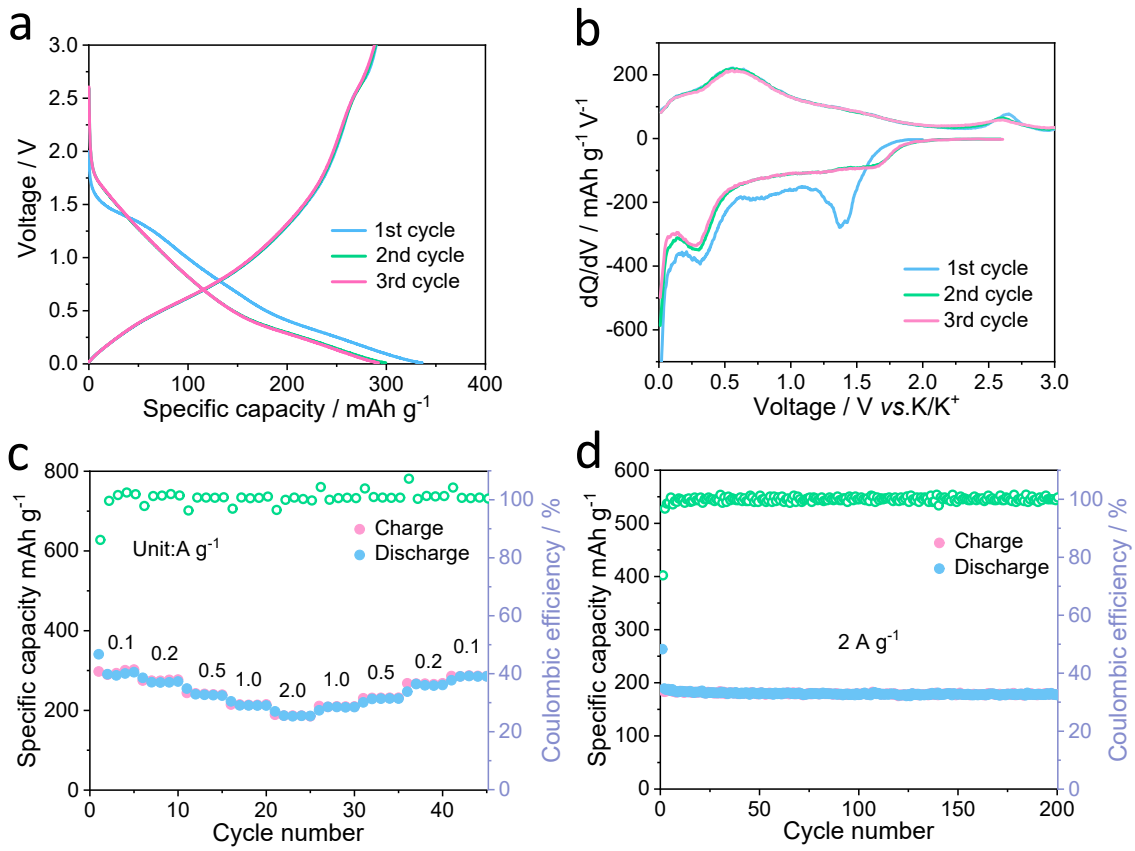


**Fig. S6** Electrochemical evaluation of the freestanding CNS. (a) Galvanostatic charge/ discharge profiles at 0.1 A $g^{-1}$. (b) The dQ/dV plots derived from the charge/discharge profiles at 0.1 A $g^{-1}$. (c) Rate capabilities ranging from 0.1 to 2.0 A $g^{-1}$. (d) Prolonged cycle life and Coulombic efficiency at 2.0 A $g^{-1}$.

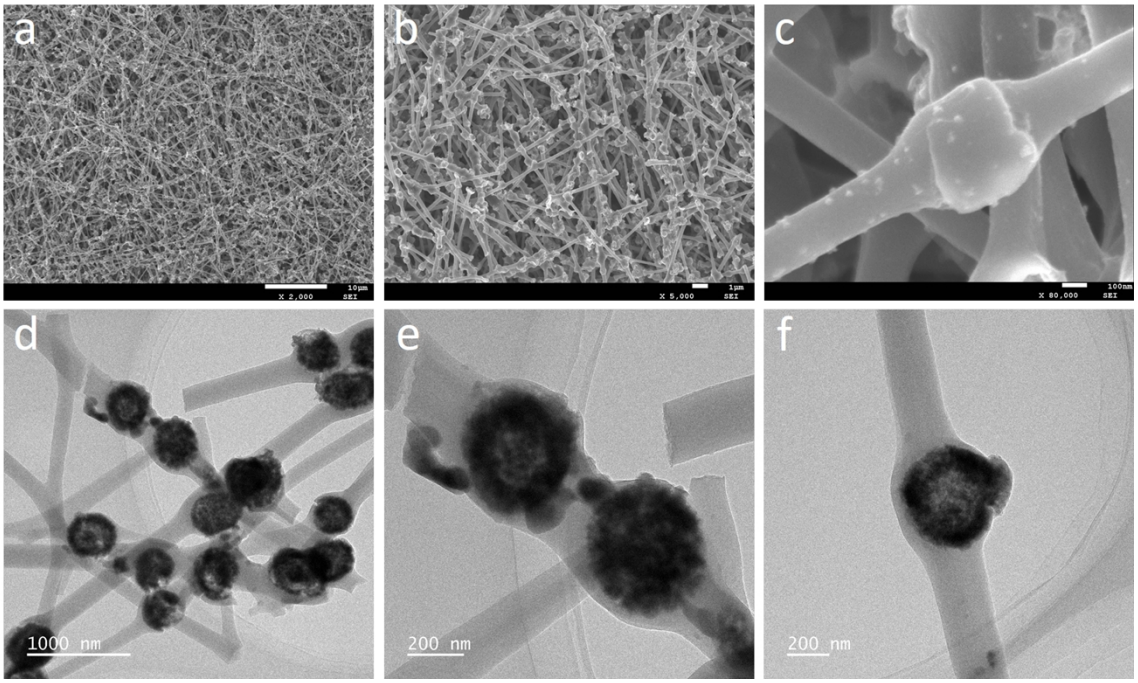


**Fig. S7** (a-c) SEM and (d-f) TEM images of the freestanding ZnSe/NiSe@NC electrode after 500 cycles.

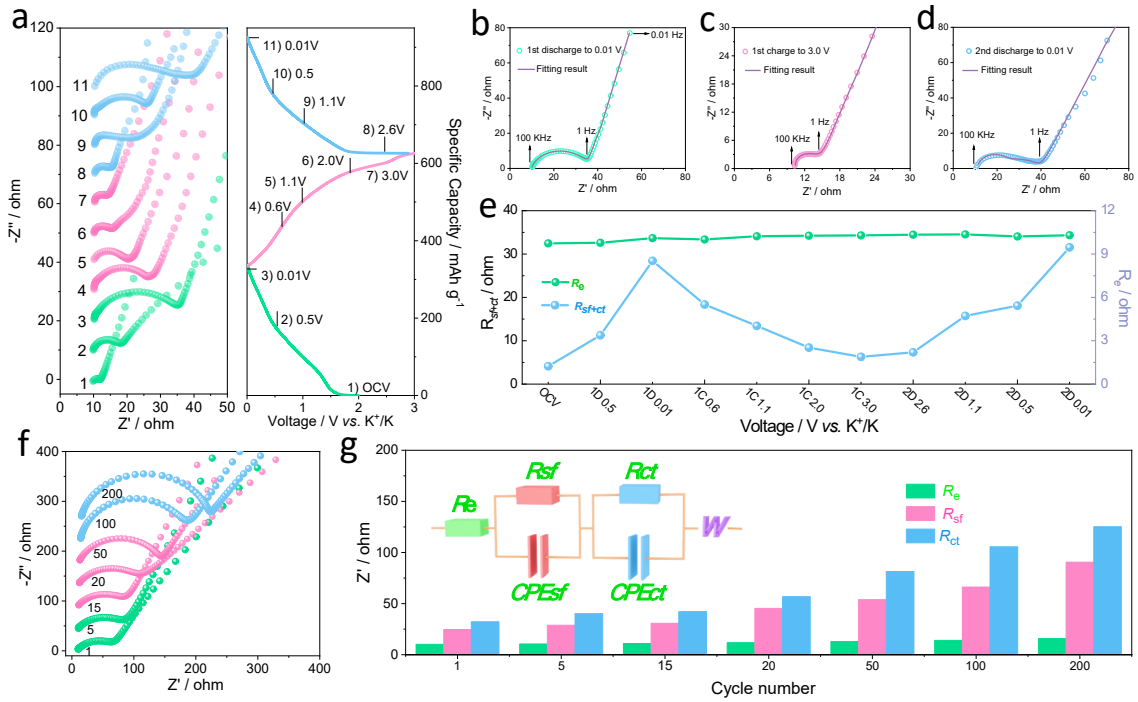


**Fig. S8** Electrochemical reaction kinetic of CNS. (a) Nyquist plots collected at different voltages in the discharge/charge process. Typical Nyquist plots collected at (b) 1st discharge to 0.01 V, (c) 1st charge to 3.0 V, and (d) 2nd discharge to 0.01 V. (e) EIS parameters derived from the equivalent circuit (inset of g). (f) Nyquist plots at full-discharged state after various cycles with a current density of 2.0 A $g^{-1}$. (g) EIS parameters at various cycles.

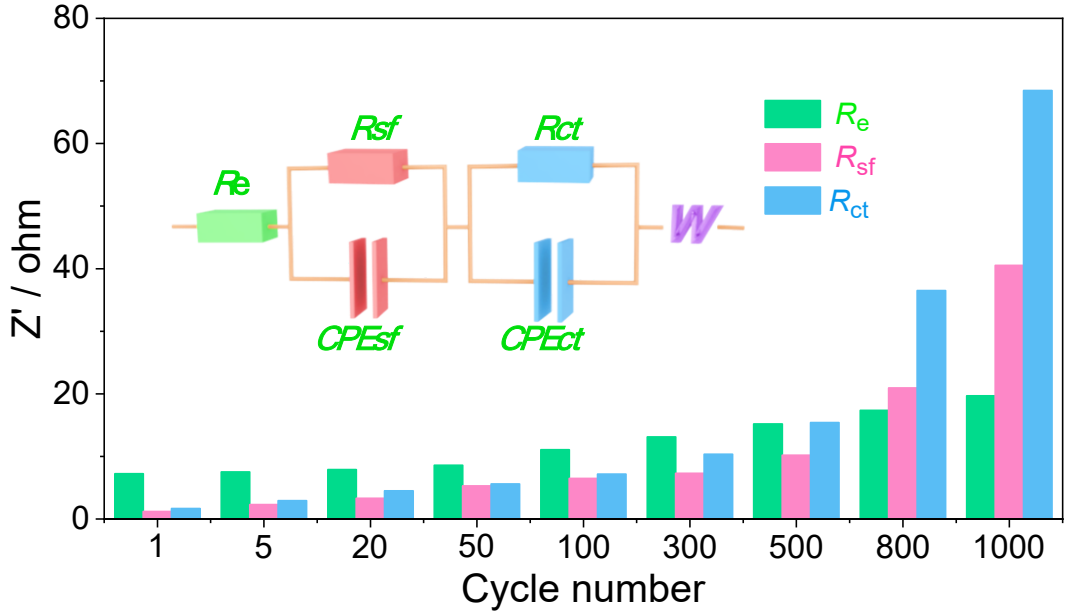


**Fig. S9** EIS parameters of ZnSe/NiSe@NC at various cycles.

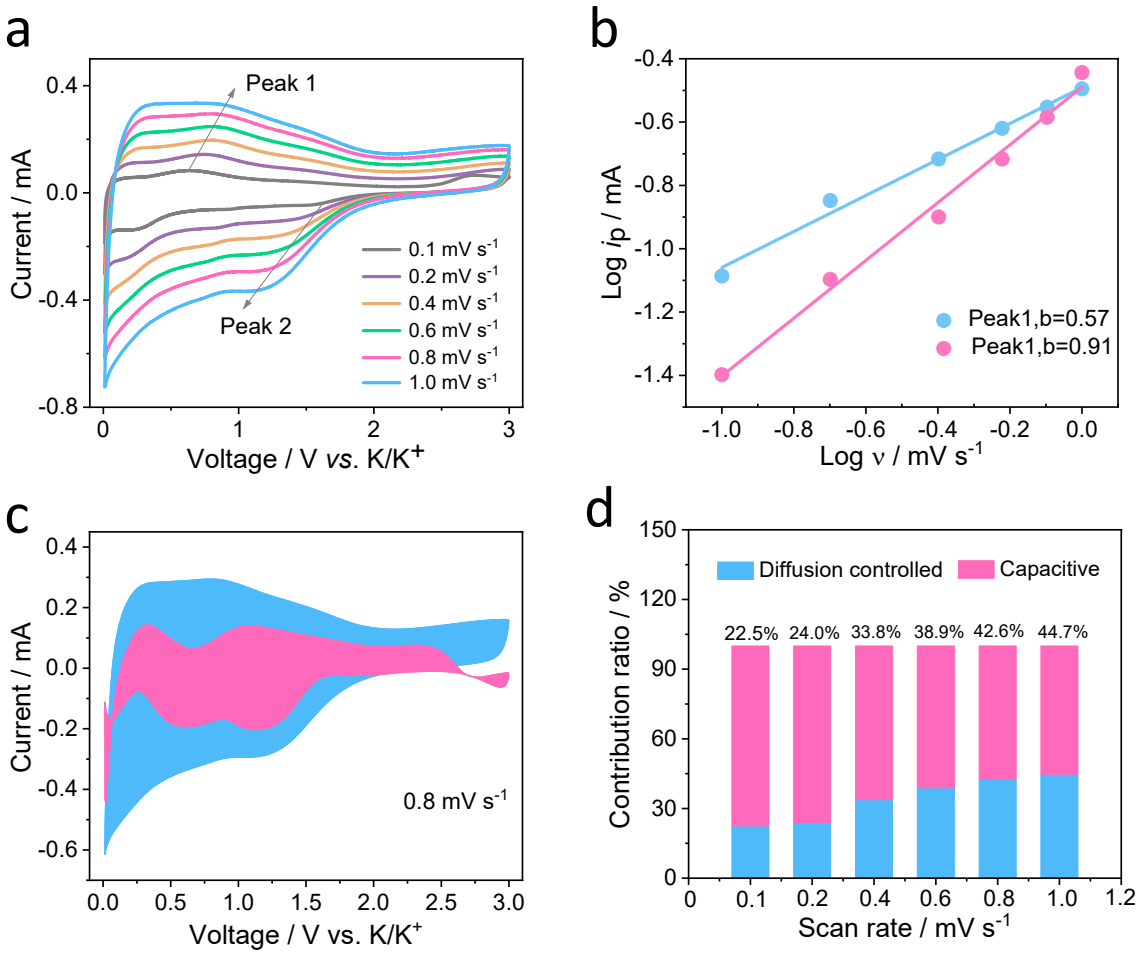


**Fig. S10** (a) CV curves of CNS at various scan rates. (b) Determination of the b value using the relationship between peak current and scan rate. (c) Separation of the capacitive and diffusion currents at a scan rate of 0.8 mV $s^{-1}$ with the capacitive fraction shown by the shaded region. (d) Contribution ratio of the capacitive and diffusion-controlled charge versus scan rate.

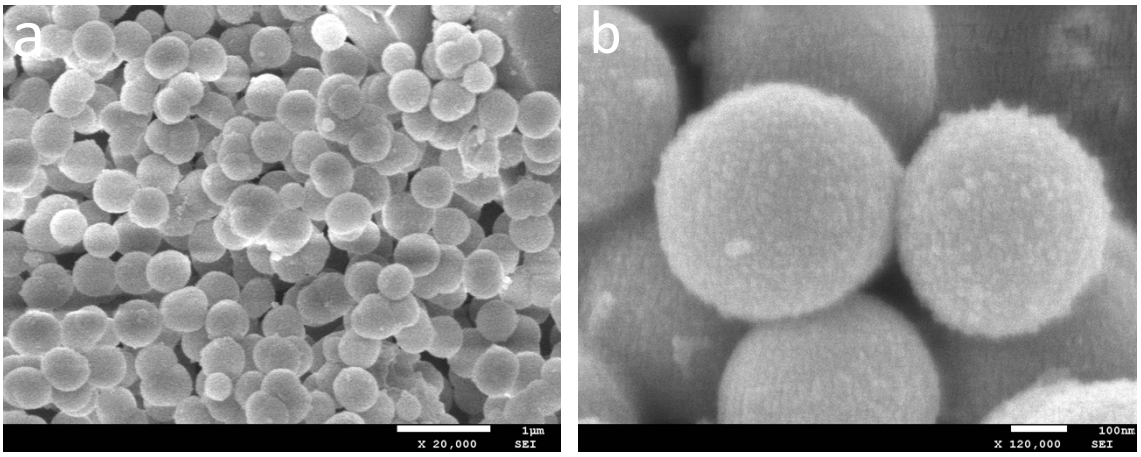


**Fig. S11** (a) Low- and (b) high-magnification SEM images of R-ZnNi-P.

.

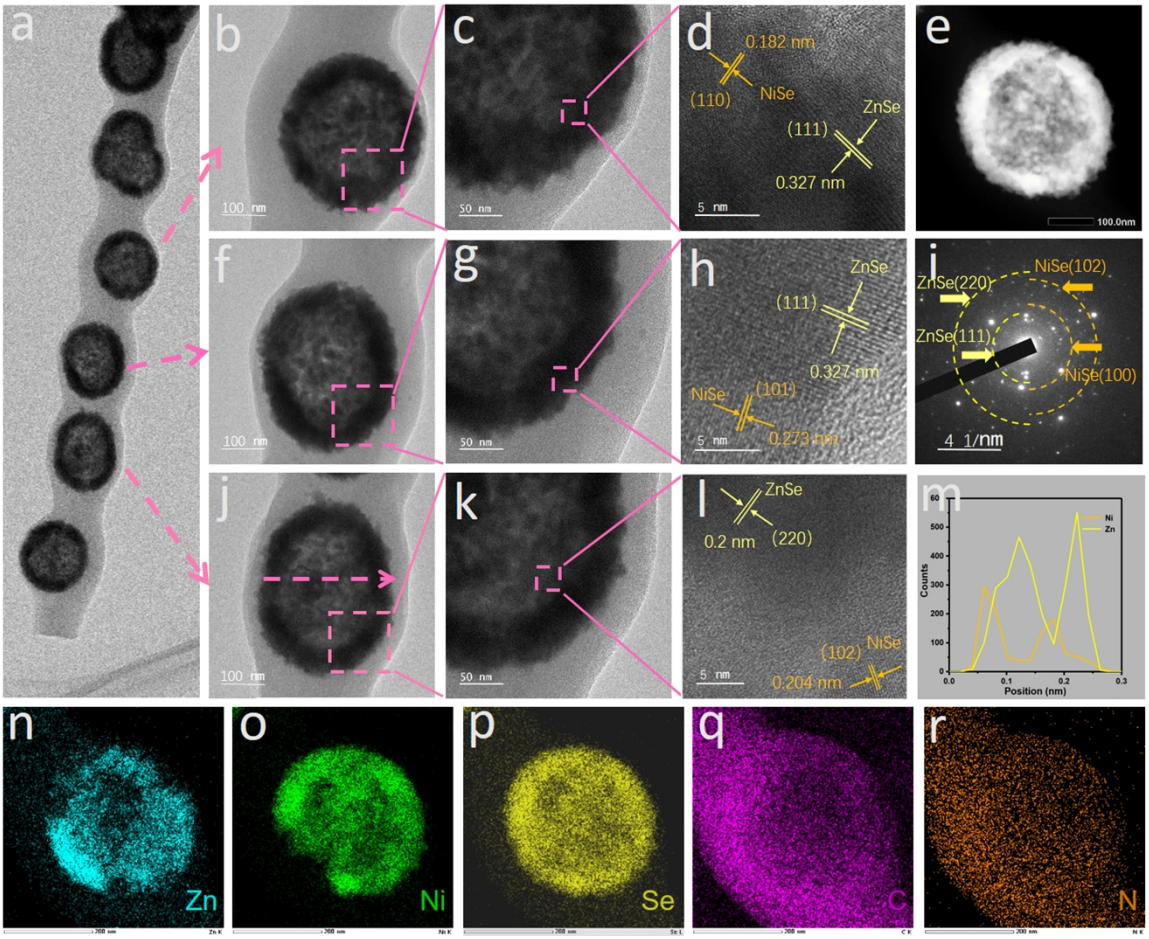


**Fig. S12** Characterization of the R-ZnSe/NiSe@NC. (a-c, f, g, j, k) TEM images and (d, h, l) HRTEM images. (e) Dark-field STEM-HADDF image and (n-r) corresponding elemental mappings. (i) SAED image and (m) EDS linear scanning result.

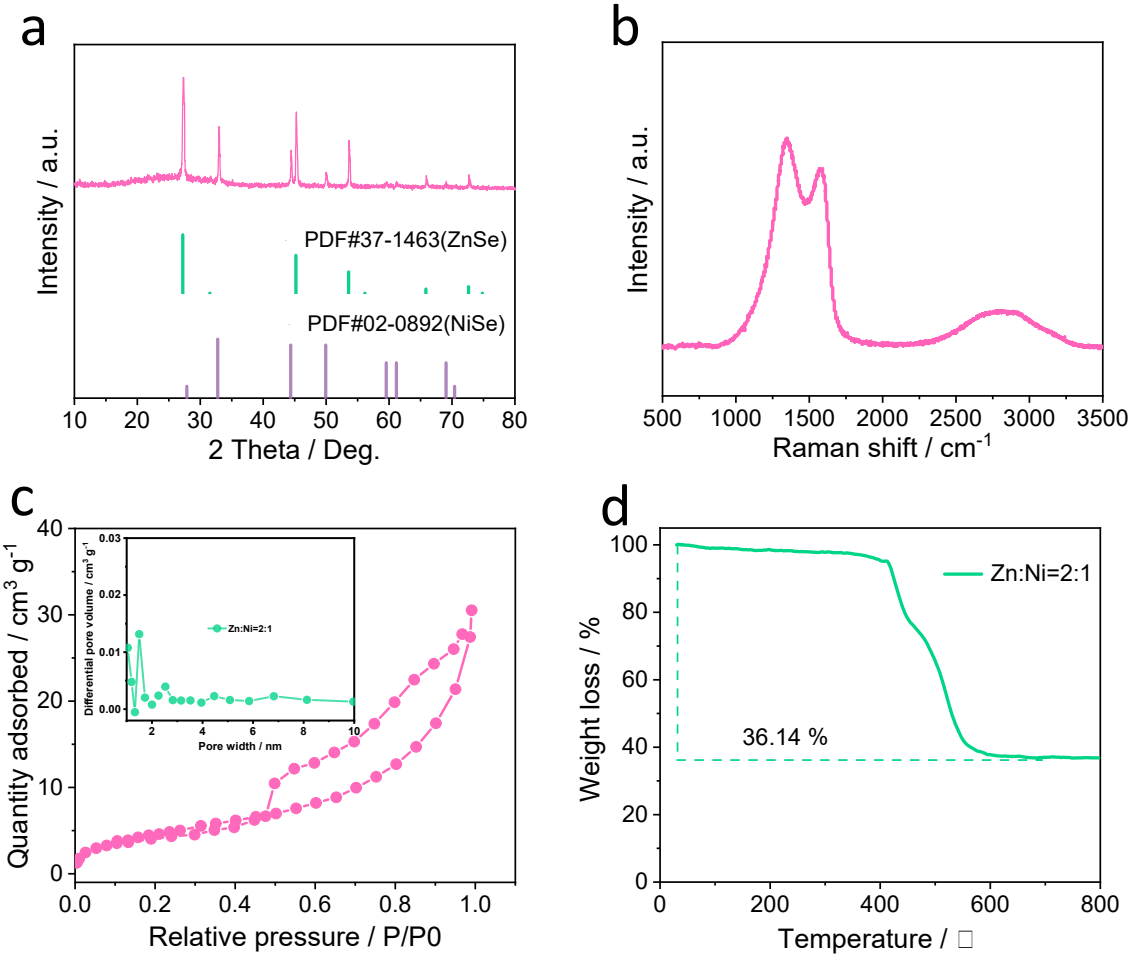


**Fig. S13** (a) XRD pattern, (b) Raman spectrum, (c) $N_2$ adsorption-desorption isotherms, and (d) TGA curve of the R-ZnSe/NiSe@NC.

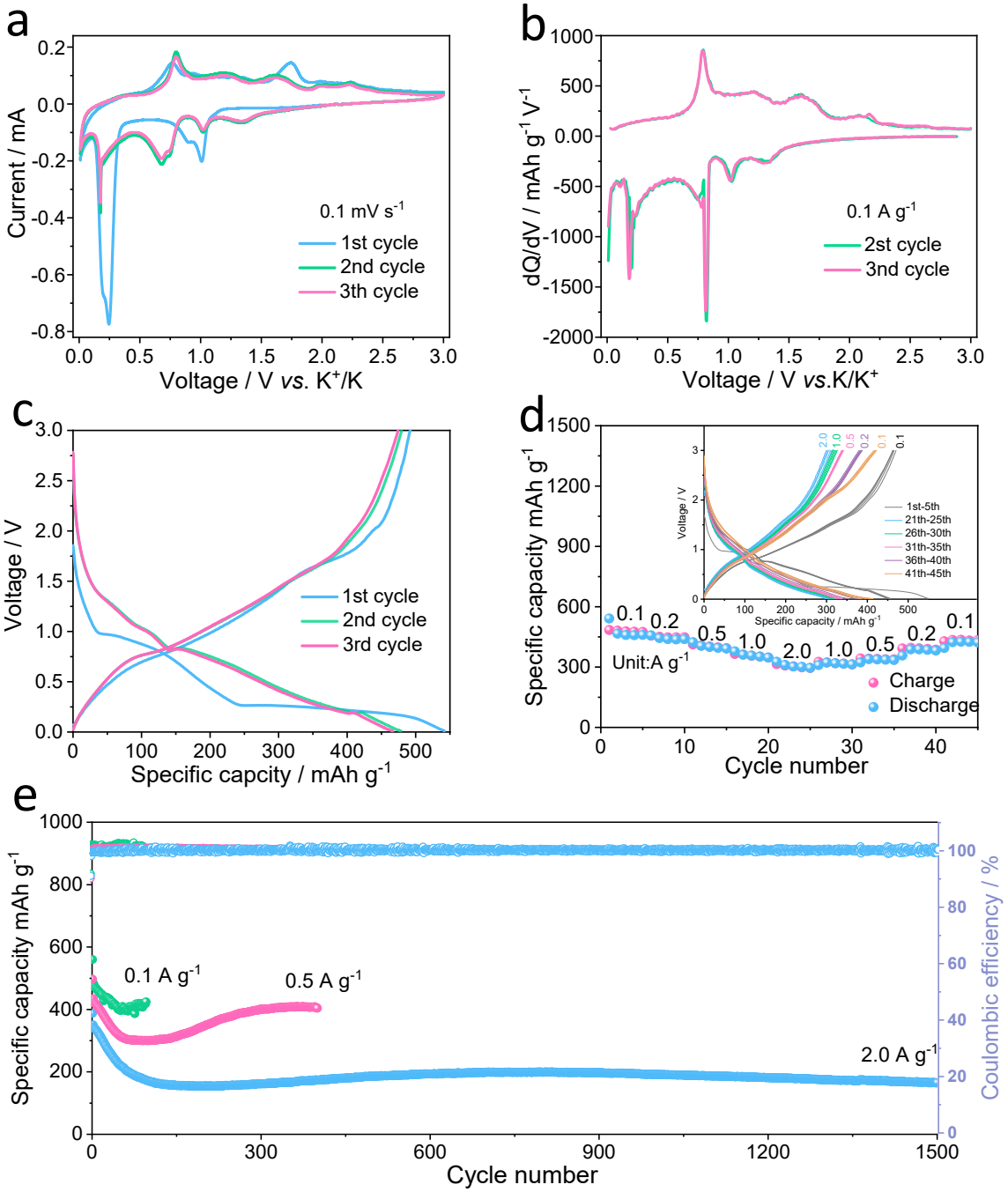


**Fig. S14** Electrochemical performance of R-ZnSe/NiSe@NC. (a) CV curves at 0.1 mV $s^{-1}$. (b) The dQ/dV plots derived from the charge/discharge profiles. (c) Galvanostatic charge/discharge profiles at 0.1 A $g^{-1}$. (d) Rate capabilities ranging from 0.1 to 2.0 A $g^{-1}$. (e) Prolonged cycle life and Coulombic efficiency at 0.1, 0.5, and 2.0 A $g^{-1}$.

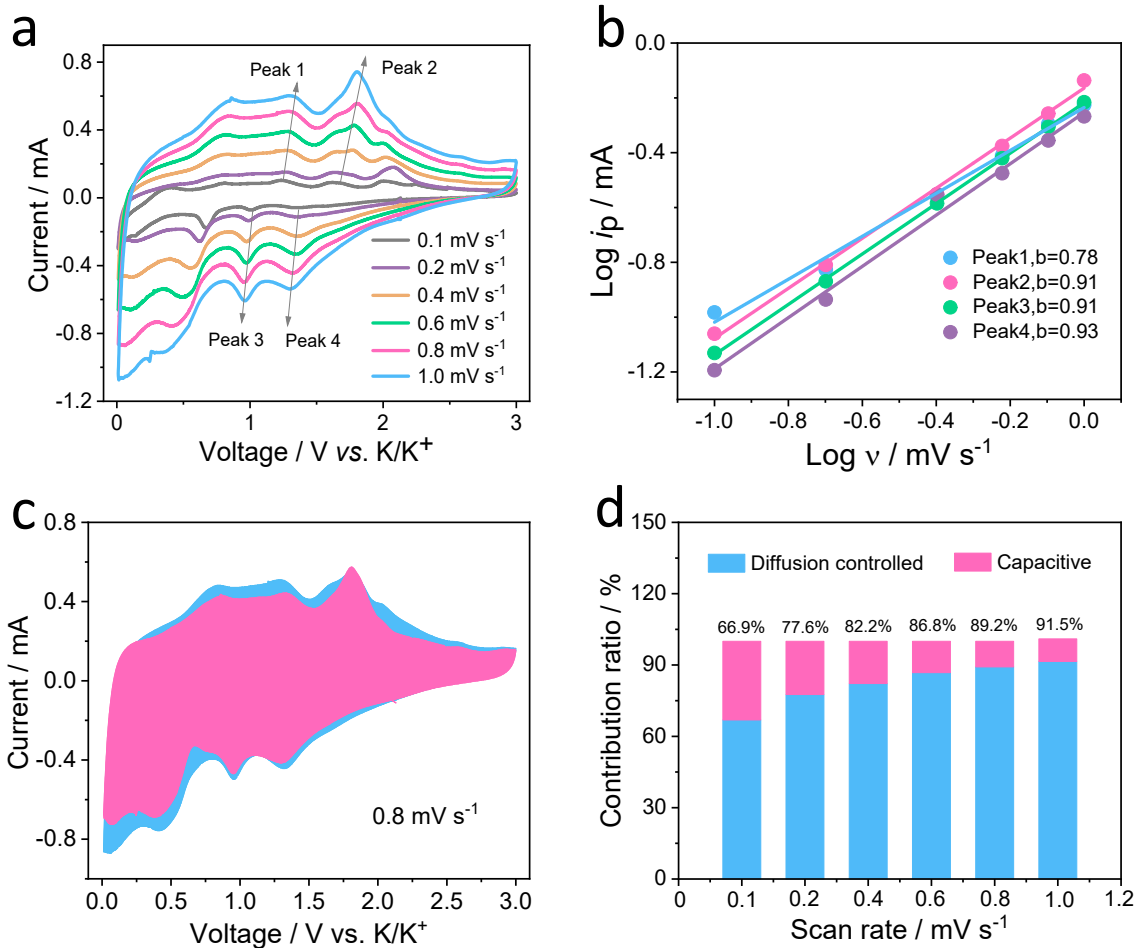


**Fig. S15** (a) CV curves of R-ZnSe/NiSe@NC at various scan rates. (b) Determination of the b value using the relationship between peak current and scan rate. (c) Separation of the capacitive and diffusion currents at 0.8 mV $s^{-1}$ with the capacitive fraction shown by the shaded region. (d) Contribution ratio of the capacitive and diffusion-controlled charge versus scan rate.

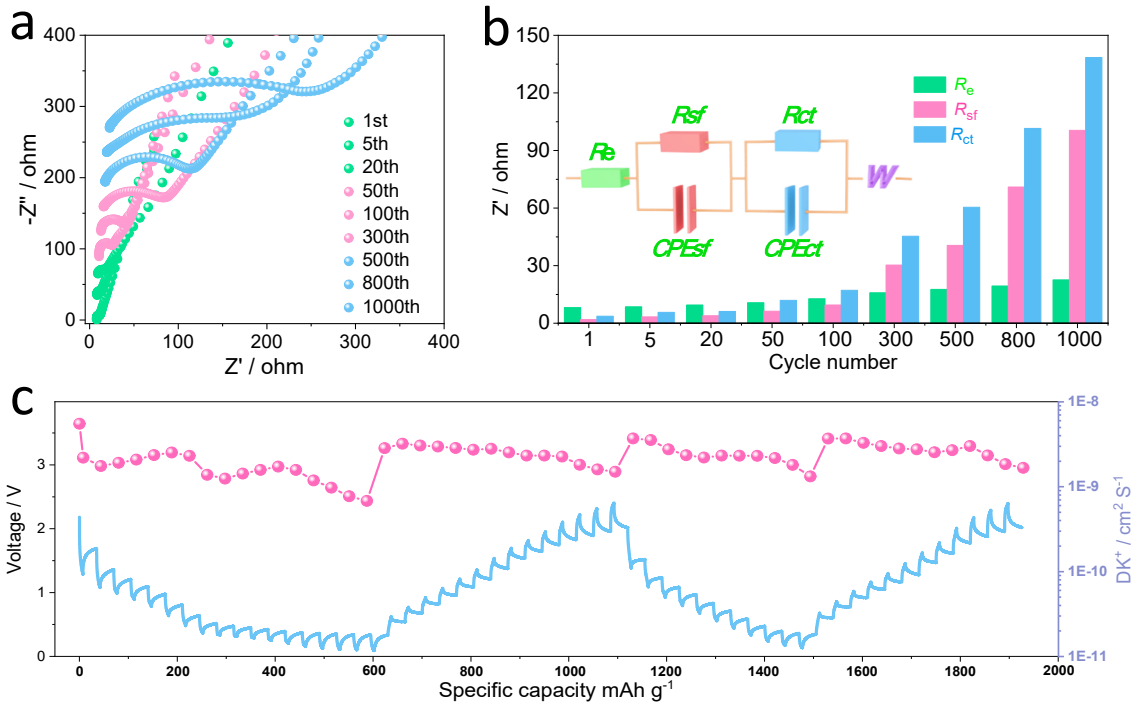


**Fig. S16** (a) Nyquist plots of R-ZnSe/NiSe@NC electrode at full-discharged state after various cycles with a current density of 2.0 A $g^{-1}$. (b) EIS parameters at various cycles. (c) GITT curves and $K^+$ diffusion coefficients of R-ZnSe/NiSe@NC electrode.

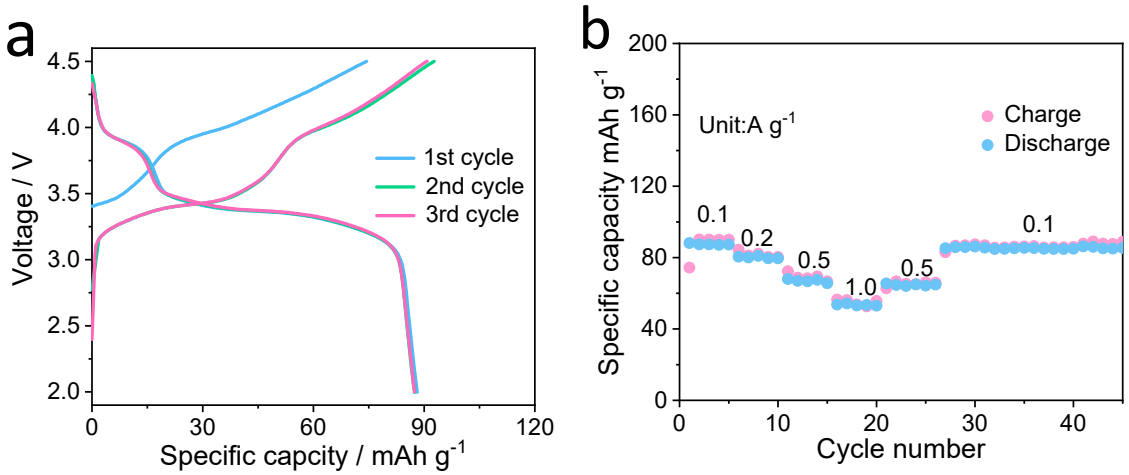


**Fig. S17** Electrochemical evaluation of $K_2FeFe(CN)_6$ cathode. (a) Galvanostatic charge/discharge profiles at 0.1 A $g^{-1}$. (b) Rate capabilities ranging from 0.1 to 1.0 A $g^{-1}$.

**Table S1.** Comparison of the reported anode performance for flexible potassium-ion batteries.

| Sample | Initial coulombic efficiency (%) | Cut-off Voltage (V) | Cyclability (mAh $g^{-1}$) /Current density (A $g^{-1}$) /Cycles | Reference |
|---|---|---|---|---|
| ZnSe/NiSe@NC | 91.6 | 0.01-3.0 | 456.3/0.1/100<br>425.9/0.5/500<br>305.6/2.0/1500 | This work |
| $SnS_2$@C-2 | 61 | 0.01-3.0 | 183.1/2.0/1000 | S1 |
| $CoTe_2$/MXene | 72.9 | 0.01-2.6 | 373.7/0.2/200 | S2 |
| KTO/rGO | 24 | 0.05-2.5 | 75/2.0/700 | S3 |
| HC-MX | 42.8 | 0.01-3.0 | 210/0.05/100 | S4 |
| $V_2C$-$VO_2$ | 75 | 0.01-3.0 | 200/1.0/2000 | S5 |
| NCNF@$CoSe_2$ | 67.9 | 0-2.5 | 253/0.2/100 | S6 |
| CDs@rGO | 44.5 | 0.01-3.0 | 244/0.2/840 | S7 |
| MoP@NPCNF | 40 | 0.01-3.0 | 280/0.1/200 | S8 |
| CNFF | 79.3 | 0.01–2.8 | 158/1.0/2000 | S9 |
| NCSCNT | 67.1 | 0-2.5 | 236/0.02/100 | S10 |
| P-rGO@M-NF | 49.5 | 0.01–2.5 | 361.2/0.1/125 | S11 |
| $SeS_2$@NCNFs | 60 | 0.5-2.8 | 417/0.5/1000 | S12 |
| M-KTO | 57.3 | 0.01-3.0 | 151/0.05/900 | S13 |
| $Co_{0.85}Se$@CNFs | 53.3 | 0.01–2.60 | 353/0.2/100 | S14 |
| $ReS_2$/N-CNFs | 64.2 | 0.01–3 | 253/0.05/100 | S15 |
| P–C NRs/CC | 64.5 | 0.01–2.5 | 388.8/0.5/400 | S16 |

**Table S2.** Comparison of the reported metal selenide anode performance for potassium-ion batteries.

| Sample | Initial coulombic efficiency (%) | Cut-off Voltage (V) | Cyclability (mAh $g^{-1}$) /Current density (A $g^{-1}$) /Cycles | Reference |
|---|---|---|---|---|
| ZnSe/NiSe@NC | 91.6 | 0.01-3.0 | 456.3/0.1/100<br>425.9/0.5/500<br>305.6/2.0/1500 | This work |
| ZnSe@i-NMC@rGO | 63.2 | 0.01-3.0 | 233.4/2.0/1500 | S17 |
| MoSe@CCS | 79.2 | 0.01-2.5 | 226/1.0/1000 | S18 |
| $CoSe_2/FeSe_2$@C | 73.1 | 0.01-2.20 | 271.4/2.0/300 | S19 |
| CPL-CuSe | 90 | 0.01-3.0 | 281/2.0/360 | S20 |
| CoSe@NC | 95 | 0.01-3.0 | 282/2.0/500 | S21 |
| $BiSbSe_3$ | 60.5 | 0.01-3.0 | 195.2/0.5/1000 | S22 |
| Mn-doped ZnSe | 73.4 | 0.01-3.0 | 167/2.0/1000 | S23 |
| $Bi_{0.48}Sb_{1.52}Se_3$@C | 57.8 | 0.01-3.0 | 223.5/1.0/1000 | S24 |
| S,P-NiSe/C | 48.3 | 0.01-3.0 | 200/0.2/500 | S25 |
| $Sn_{0.95}Cu_{0.05}Se$@CNF | 62.3 | 0.01-3.0 | 224/0.5/500 | S26 |
| $CoSe_2$-$Cu_2Se$@NC | 90.5 | 0.01-3.0 | 325.4/1.0/120 | S27 |
| αMnSe@NC@GO | 62.0 | 0.01-3.0 | 92.6/1.0/700 | S28 |
| $MoSe_2$/C/rGO | 75.7 | 0.01-3.0 | 307/1.0/1000 | S29 |
| SnSe/3D RGO@NC | 57.2 | 0.01-3.0 | 192/2.0/300 | S30 |
| $VSe_2$@CQD | 48.2 | 0.01-3.0 | 196.4/0.5/1000 | S31 |
| Zn-Mn-Se@FC | 84.2 | 0.15-3.0 | 227/2.0/500 | S32 |
| $WSe_2$@NC | 64.5 | 0.01-2.6 | 122.1/0.5/1300 | S33 |

**Calculation of metal selenide content**

According to previous reports (DOI: 10.1016/j.jpowsour.2020.227937 and 10.1016/j.ensm.2019.10.013), the final products of the ZnSe/NiSe@NC material after heat treatment in air are ZnO and NiO, with the following reaction equations:

$$NiSe(s) + O_2(g) \rightarrow NiO(s) + SeO_2(g) \quad (1)$$

$$ZnSe(s) + O_2(g) \rightarrow ZnO(s) + SeO_2(g) \quad (2)$$

$$C(s) + O_2(g) \rightarrow CO_2(g) \quad (3)$$

Based on the TGA results shown in Fig. 3c, the mass percentage of the remaining products ZnO and NiO is 36.18 wt%. Noth that the molar ratio of ZnO (81.38 g $mol^{-1}$) to NiO (74.69 g $mol^{-1}$) is consistent with that of ZnSe (144.35 g $mol^{-1}$) to NiSe (137.66 g $mol^{-1}$), determined to be approximately 1:2 by inductively coupled plasma optical emission spectrometry (ICP-OES). Therefore, if we assume the molar quantity of ZnO is *x*, the mass percentage of metal selenides in the ZnSe/NiSe@NC composite can be easily calculated using the following equation.

$$\omega_{ZnO/NiO} = \frac{m_{ZnO} + m_{NiO}}{m_C + m_{ZnSe} + m_{NiSe}} = \frac{81.38 + 2*74.69}{\frac{m_C}{x} + 144.35 + 2*137.66} = 36.18\ wt\% \quad (4)$$

$$\omega_{ZnSe/NiSe} = \frac{m_{ZnSe} + m_{NiSe}}{m_C + m_{ZnSe} + m_{NiSe}} = \frac{144.35 + 2*137.66}{\frac{m_C}{x} + 144.35 + 2*137.66} = 65.80\ wt\% \quad (5)$$

**Density functional theory (DFT)**

All the DFT calculations were conducted based on the Vienna Ab-inito Simulation Package (VASP).[34, 35] The exchange-correlation effects were described by the Perdew-Burke-Ernzerhof (PBE) functional within the generalized gradient approximation (GGA) method.[36, 37] The core-valence interactions were accounted by the projected augmented wave (PAW) method.[38] The energy cutoff of 450 eV used in this work. Meanwhile, the k-mesh for NiSe, ZnSe and NiSe/ZnSe slab models employed in the first irreducible Brillouin zone were 3 × 2 × 1, 2 × 2 × 1 and 2 × 1 × 1, respectively. It is worth mentioning that the vacuum spacing of 15 Å used in the slab models. The structural optimization was completed for energy and force convergence set at $1.0\times10^{-5}$ eV and 0.03 eV $Å^{-1}$, respectively. The climbing-image nudged elastic band (CI-NEB) method was employed to locate the transition states (TS) of K atom migration.[39, 40] The image number of the CI-NEB calculations was obtained based on a calculated reference value: the VASP-VTST script calculated the atomic distance between the initial and final states.[41]

**References**


S1 D. Li, L. Dai, X. Ren, F. Ji, Q. Sun, Y, Zhang and L. Ci, *Energy Environ. Sci.*, 2021, **14**, 424–436.

S2 X. Xu, Y. Zhang, H. Sun, J. Zhou, Z. Liu, Z. Qiu and S. Guo, *Adv. Mater.*, 2021, **33**, 2100272.

S3 C. Zeng, F. Xie, X. Yang, M. Jaroniec, L. Zhang and S. Z. Qiao, *Angew. Chem. Int. Ed.*, 2018, **130**, 8676–8680.

S4 Sun, Q. Zhu, B. Anasori, P. Zhang, H. Liu, Y. Gogotsi and B. Xu, *Adv. Funct. Mater.*, 2019, **29**, 1906282.

S5 M. Xu, D. Zhou, T. Wu, J. Qi, Q. Du and Z. Xiao, *Adv. Funct. Mater.*, 2022, **32**, 2203263.

S6 Q. Yu, B. Jiang, J. Hu, C. Y. Lao, Y. Gao, P. Li and G. Yin, *Adv. Sci.*, 2018, **5**, 1800782.

S7 E. Zhang, X. Jia, B. Wang, J. Wang, X. Yu and B. Lu, *Adv. Sci.*, 2020, **7**, 2000470.

S8 Z. Yi, Y. Liu, Y. Li, L. Zhou, Z. Wang, J. Zhang and Z. Lu, *Small*, 2020, **16**, 1905301.

S9 H. Li, Z. Cheng, Q. Zhang, A. Natan, Y. Yang, D. Cao and H. Zhu, *Nano Lett.*, 2018, **18**, 7407–7413.

S10 X. Zhao, Y. Tang, C. Ni, J. Wang, A. Star and Y. Xu, *ACS Appl. Energy Mater.*, 2018, **1**, 1703–1707.

S11 X. Lu, W. L. Lin, Y. E. Huang, J. X. Zhang, L. H. Guan, X. Y. Huang and X. H. Wu, *ACS Appl. Energy Mater.*, 2021, **4**, 9682–9691.

S12 Y. Yao, R. Xu, M. Chen, X. Cheng, S. Zeng, D. Li and Y. Yu, *ACS Nano*, 2019, **13**, 4695–4704.

S13 Y. Dong, Z. S. Wu, S. Zheng, X. Wang, J. Qin, S. Wang and X. Bao, *ACS Nano*, 2017, **11**, 4792–4800.

S14 C. A. Etogo, H. Huang, H. Hong, G. Liu and L. Zhang, *Energy Storage Mater.*, 2020**, 24**, 167–176.

S15 M. Mao, C. Cui, M. Wu, M. Zhang, T. Gao, X. Fan and C. Wang, *Nano Energy*, 2018, **45**, 346–352.

S16 J. Li, W. Qin, J. Xie, H. Lei, Y. Zhu, W. Huang and W. Mai, *Nano Energy*, 2018, **53**, 415–424.

S17 J. Ruan, J. Zang, J. Hu, R. Che, F. Fang, F. Wang and D. Sun, *Adv. Sci.*, 2022, **9**, 2104822.

S18 W. Wang, B. Jiang, C. Qian, F. Lv, J. Feng, J. Zhou and S. Guo, *Adv. Mater.*, 2018, **30**, 1801812.

S19 H. Shan, J. Qin, Y. Ding, H. M. K. Sari, X. Song, W. Liu and X. Li, *Adv. Mater.*, 2021, **33**, 2102471.

S20 H. Lin, M. Li, X. Yang, D. Yu, Y. Zeng, C. Wang and F. Du, *Adv. Energy Mater.*, 2019, **9**, 1900323.

S21 Y. Liu, Q. Deng, Y. Li, Y. Li, W. Zhong, J. Hu and K. Huang, *ACS Nano*, 2021, **15**, 1121.

S22 W. C. Lin, Y. C. Yang and H. Y. Tuan, *Energy Storage Mater*., 2022, **51**, 38–53.

S23 S. Liang, Z. Yu, T. Ma, H. Shi, Q. Wu, L. Ci and Z. Xu, *ACS Nano*, 2021, **15**, 14697–14708.

S24 T. Yuan, J. Yan, Q. Zhang, Y. Su, S. Xie, B. Lu and X. Ouyang, *ACS Nano*, 2023, **17**, 10462–10473.

S25 J. Ye, Z. Chen, Z. Zheng, Z. Fu, G. Gong, G. Xia and C. Hu, *J. Energy Chem.*, 2023, **78**, 401.

S26 N. Ren, L. Wang, J. Dong, K. Cao, Y. Li, F. Chen and C. Chen, *Chem. Eng. J*., 2023, **458**, 141489.

S27 X. Liu, Z. Niu, Y. Xu, Z. Zhao, C. Li, Y. Yi and D. Li, *Chem. Eng. J.*, 2022, **430**, 133176.

S28 T. Li, Y. Wang, L. Yuan, Q. Zhou, S. Qiao, Z. Liu and S. Chong, *Chem. Eng. J.*, 2022, **446**, 137152.

S29 D. Xu, L. Chen, X. Su, H. Jiang, C. Lian, H. Liu and C. Li, *Chem. Eng. J.*, 2022, **32**, 2110223.

S30 F. Wang, J. Huang, L. Cao, J. Su, K. Kajiyoshi, Y. Liu and J. Li, *Carbon*, 2023, **204**, 126–135.

S31 Y. Feng, C. Xu, K. Wu, Y. Guo, S. Wu, Z. Guo and M. Xue, *ACS Appl. Nano Mater.*, 2022, **5**, 13136–13148.

S32 P. Zhou, M. Zhang, L. Wang, Q. Huang, Z. Su, P. Xu and K. Ba, *Small*, 2022, **18**, 2203964.

S33 X. Chen, H. Muheiyati, X. Sun, P. Zhou, P. Wang, X. Ding and L. Xu, *Small*, 2022, **18**, 2104363.

S34 G. Kresse and J. Hafner, *Phys. Rev. B*, 1993, **47**, 558–561.

S35 G. Kresse and J. Hafner, *Phys. Rev. B*, 1994, **49**, 14251–14269.

S36 J. P. Perdew, K. Burke and M. Ernzerhof, *Phys. Rev. Lett.*, 1996, **77**, 3865–3868.

S37 G. Kresse and D. Joubert, *Phys. Rev. B*, 1999, **59**, 1758–1775.

S38 P. E. Blöchl, *Phys. Rev. B*, 1994, **50**, 17953–17979.

S39 G. Henkelman and H. Jónsson, *J. Chem. Phys.*, 2000, **113**, 9978–9985.

S40 G. Henkelman, B. P. Uberuaga and H. Jónsson, *J. Chem. Phys.*, 2000, **113**, 9901–9904.

S41 G. Kresse and J. Hafner, *J. Non–Cryst. Solids*, 1993, **47**, 558.